JOURNAL OF SPACECRAFT AND ROCKETS
Vol. 43, No. 6, November–December 2006

Midcourse Space Experiment: Off-Axis Rejection Performance of the Infrared Sensor

Robert R. O'Neil* and James Gibson†
U.S. Air Force Research Laboratory, Hanscom Air Force Base, Bedford, Massachusetts 01731
and
Edward Richards‡
Boston College, Chestnut Hill, Massachusetts 02467

The Spatial Infrared Imaging Telescope III (SPIRIT III) sensor on the Midcourse Space Experiment (MSX) satellite observed stray radiation from the lower atmosphere and terrestrial surface, nonrejected Earth radiance, at angles of approximately 2 to 14 deg from the optical axis in measurements of Earth limb radiance. Analysis indicates that direct scatter of terrestrial radiance from contaminants on the telescope primary mirror is the principal source of stray radiation and the bidirectional reflectance distribution function (BRDF) of the primary mirror for the 6.8–10.8-μm radiometer band is $(1.11 \pm 0.22) \times 10^{-2}$ per sr at 1 deg off axis with an angular dependence of $\theta^{-1.71 \pm 0.07}$. Similarly, the BRDF values for the three other LWIR radiometer bands (11.1–13.2, 13.5–15.9, and 18.2–25.1 μm) have been determined as $(1.03 \pm 0.05) \times 10^{-2}\theta^{-1.66 \pm 0.10}$, $(2.21 \pm 0.18) \times 10^{-2}\theta^{-2.04 \pm 0.21}$, and $(2.59 \pm 0.02) \times 10^{-2}\,\theta^{-2.10 \pm 0.09}$ sr^{-1}, respectively. The BRDF values derived from the on-orbit data are significantly greater than prelaunch measurements, and the increase is attributed to particulate accumulation on the primary mirror during the prelaunch period, launch, and the on-orbit telescope aperture cover removal and ejection process.

Nomenclature

B_1	=	bidirectional reflectance distribution function (BRDF) coefficient for the primary mirror, sr^{-1}
B_2	=	BRDF coefficient for the secondary mirror, sr^{-1}
D	=	limiting (circular) diffraction aperture diameter, μm
$L(\theta, \phi)$	=	terrestrial and atmospheric radiance, W cm^{-2}sr^{-1}
m_1	=	angular exponential term of direct scatter from the primary mirror
m_2	=	angular exponential term of direct scatter from the secondary mirror
n_1	=	angular exponential term of indirect scatter from the primary mirror
n_2	=	angular exponential term of indirect scatter from the secondary mirror
r	=	particle radius, μm
sr	=	solid angle, steradians
T	=	absolute temperature, K
x	=	particle size parameter
θ	=	angle measured from the optical axis, deg
λ	=	wavelength of radiation, μm
$\langle\lambda\rangle$	=	average wavelength of radiometer spectral band, μm
ϕ	=	azimuth angle measured in a plane normal to the optical axis, deg

I. Introduction

THE Midcourse Space Experiment, a Missile Defense Agency (formerly the Ballistic Missile Defense Organization) research program to support the development of advanced surveillance systems, successfully completed 150 measurements of infrared atmospheric radiance and spatial structure in Earth limb scenes as part of an extensive series of target and background measurements. The episodic Earth limb measurements were nominally about 30 min in duration, were performed primarily at tangent heights ranging from 30 to 150 km, and included brief segments with scans down from and up to a tangent height of 900 km at the beginning and conclusion of each data collection event. At higher tangent heights, the SPIRIT III sensor observed stray light or nonrejected Earth radiance (NRER) from the intense emission of the lower atmosphere and the terrestrial surface, which appeared as an extended off-axis source beyond the 1-deg field of view of the SPIRIT III radiometer. The NRER, which exceeded on-axis atmospheric radiance at tangent heights above 90–150 km (depending on spectral band), was characterized by a decrease with increasing altitude and was evident as high as 900 km in the four SPIRIT III radiometer long-wavelength infrared (LWIR) bands. The MSX satellite (Fig. 1) was launched on 24 April 1996 into a nearly sun-synchronous orbit at 900 km, and episodic infrared measurements continued until the cryogenic supply of solid hydrogen was depleted on 25 February 1997.

The MSX program[1] successfully completed many different types of experiments including observations of ultraviolet, visible and infrared atmospheric,[2,3] terrestrial,[4] and celestial[5] backgrounds; contamination levels of spacecraft surfaces and the local environment[6]; and infrared standard reference stars and well-characterized deployed objects to calibrate and monitor the performance of the MSX sensors.[7] The MSX program objectives, sensors, and experiments are described in Ref. 1. The primary MSX sensor, SPIRIT III, included an LWIR radiometer that provided simultaneous infrared measurements in four discrete wavelength bands: 6.8–10.8, 11.1–13.2, 13.5–15.9, and 16.2–25.1 μm. Table 1 indicates the low-altitude measurement limit for each band as set by saturation caused by atmospheric emissions in the mesosphere and lower stratosphere. Bands A and D saturate at higher altitudes because of the intense emission of the atmospheric 9.6 μm O_3 and 15 μm CO_2 bands, respectively. SPIRIT III also included two midwavelength infrared (MWIR) radiometer bands and an interferometer spectrometer. However, as anticipated, the NRER in the MWIR bands was below the detection threshold, and NRER, as measured by the interferometer, is beyond the scope of the results presented here.

The angular separation of the SPIRIT III boresight at a tangent height of 100 km and the Earth's horizon was approximately 1.7 deg.

Received 19 August 2005; revision received 18 November 2005; accepted for publication 28 November 2005.

*Research Physicist, Battlespace Environment Division, Space Vehicles Directorate, VSBYB. Member AIAA.
†Research Physicist, Battlespace Environment Division, Space Vehicles Directorate, VSBYB.
‡Senior Scientist, Institute for Scientific Research, 140 Commonwealth Avenue.

Table 1 MSX LWIR radiometer bands

Band	FWHM, μm[a]	Low-altitude limit, km
A	6.8–10.8	57
C	11.1–13.2	25
D	13.5–15.9	63
E	18.2–25.1	25

[a]Full-width half-maximum system spectral response.

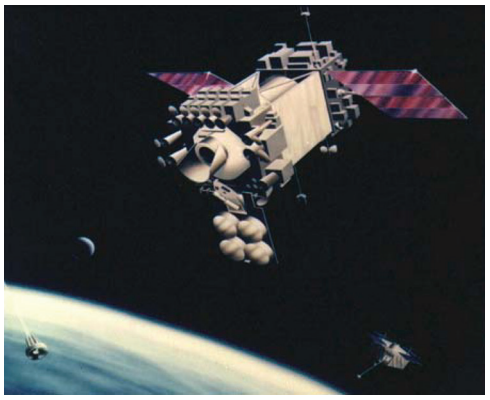

Fig. 1 The 2700-kg MSX satellite, approximately 5 × 2 m, contained a suite of ultraviolet, visible, and infrared sensors. The large sensor with the telescope Earth shield in the center of the satellite is the SPIRIT III radiometer and interferometer spectrometer.

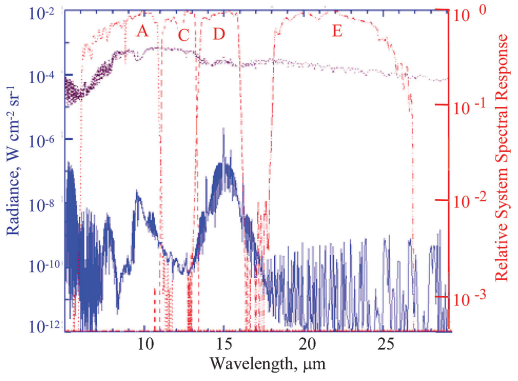

Fig. 2 Spectral radiance from the SAMM model for an equatorial day atmosphere at a tangent height of 100 km (lower trace) and cloud-free conditions for a line of sight intersecting the terrestrial surface slightly below the horizon (upper trace). The relative system response of the SPIRIT III LWIR radiometer bands is also indicated and referenced to the right-side scale.

Figure 2 illustrates a model calculation of the infrared radiance observed by a space based sensor for an above-the-horizon (ATH) line of sight with a tangent height of 100 km and for a below-the-horizon (BTH) line of sight intersecting the Earth's surface. Limb radiance increases exponentially with decreasing altitude and, as illustrated in Fig. 2, increases approximately three and six orders of magnitude from a tangent height of 100 km to the horizon for bands D and E, respectively. Thus, space-based sensors designed to observe optical and infrared emission in Earth limb views are required to reject intense radiation from the low atmosphere and terrestrial surface at small off-axis angles. NRER has been observed in high-altitude rocket-based infrared atmospheric limb and celestial measurements[8] and in the CIRRIS 1A space shuttle experiment.[9] The history of the stray light rejection capability for a number of infrared telescopes for space-based applications has been documented[10] based on periodic prelaunch measurements in test facilities.

The MSX SPIRIT III infrared sensor included design features and optical component specifications to reduce off-axis sources of stray light to support measurements of upper atmospheric limb radiance and radiance fluctuations. Stray radiation contributes to the sensor noise level and variations in the off-axis scene radiance caused by clouds can modulate the NRER, contribute low-frequency radiance fluctuations, and further degrade the performance capabilities of a space-based infrared sensor. The SPIRIT III telescope performance specifications and test results are given in Ref. 11. The afocal fore optics of the SPIRIT III telescope consisted of three super polished, gold-coated, nickel-plated aluminum mirrors with a primary mirror diameter of 36.8 cm. The SPIRIT III instrument was designed, assembled, and operated by the Space Dynamics Laboratory at Utah State University.[12] The telescope and optical system were designed and fabricated by the Sensor Systems Group, Inc.

NRER is a significant component of limb radiance in the SPIRIT III radiometer measurements in bands A, C, D, and E at tangent heights above approximately 100, 90, 150, and 80 km, respectively; it is apparent at tangent heights up to approximately 660 km and also is evident as a low signal-to-noise ratio source in some measurements at tangent heights up to 900 km. This report presents an analysis of NRER observed at altitudes in the range from approximately 90 to 660 km in the four MSX LWIR radiometer bands using the Air Force Research Laboratory radiance code, SAMM[13] (SHARC and MODTRAN Merged). SHARC, Strategic High Altitude Radiance Code, calculates infrared limb radiance at altitudes from 30 to 300 km, including the effects of nonlocal thermodynamic equilibrium, while MODTRAN (moderate resolution transmission model) is used in SAMM for altitudes below 30 km. The model of atmospheric and terrestrial radiance is used to estimate the point source rejection ratio (PSRR) of the SPIRIT III telescope and optical system. The PSRR is examined to assess the source of off-axis radiance and to characterize the bidirectional reflectance distribution function (BRDF), of the primary and secondary telescope mirrors and the coefficient of secondary scatter from these optical elements. The scattering properties of contaminants on the SPIRIT III telescope primary mirror are reported here as a BRDF for each of the four MSX LWIR radiometer bands. Lower levels of NRER, observed at tangent heights from 660 to 900 km, are believed to be caused by indirect or secondary scattering. Estimates of indirectly scattered radiance as a result of multiple reflections from the telescope baffle assembly and subsequently the primary mirror are reported in the form of an upper-limit estimate for a secondary scatter coefficient for the 6.8–10.8-μm radiometer band.

The following sections present simulations of the components of limb radiance attributed to atmospheric, zodiacal, and off-axis nonrejected Earth radiance for three levels of mirror cleanliness; simulations of the NRER components caused by diffraction and direct and indirect scatter from the SPIRIT III telescope mirrors; analysis of the on-orbit NRER data in terms of BRDF of the primary telescope mirror for the four SPIRIT III radiometer LWIR bands; and an interpretation of the magnitude of the derived BRDF values in terms of cleanliness level.

II. Limb Radiance Simulations

The infrared radiance observed by the MSX SPIRIT III radiometer in Earth limb views was estimated in prelaunch simulations to establish limb measurement capabilities, to facilitate experiment planning, to support the analysis of atmospheric emissions, and to assess the potential range of limb radiance due to atmospheric, zodiacal, and nonrejected Earth radiance for each of the SPIRIT III radiometer bands. Limb radiance simulations for the 11.1–13.2-μm LWIR radiometer band are presented in Fig. 3 for three views of the zodiacal background and three cases of mirror cleanliness. The zodiacal radiance components exceed atmospheric limb radiance at altitudes above approximately 100–120 km. The NRER values in Fig. 3 represent the three levels of mirror cleanliness given by the BRDF values of Table 2 and, for convenience, are described here as pristine, moderately contaminated, and contaminated conditions.

The prelaunch radiance estimate for each component of the limb emission, atmospheric, zodiacal, and NRER, is described in the following sections.

Table 2 BRDF values used in prelaunch simulations[a]

Case	Description	B	m
1	Pristine	1.0×10^{-4}	2
2	Moderate contamination	3.0×10^{-3}	1.5
3	Contaminated	1.0×10^{-2}	1.1

[a]BRDF $= B \times \theta^{-m}$ (sr^{-1}), where θ is the angle from the optical axis in degrees.

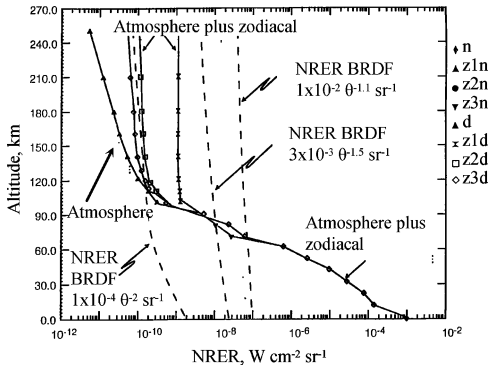

Fig. 3 Limb radiance simulations for MSX LWIR band C (11.1–13.2 μm) for day (designated d) and night (n) atmospheres, three cases of mirror cleanliness (BRDF), and three views of the zodiacal background (z1, z2, and z3). The zodiacal backgrounds have been combined with the day and night radiance profiles (z1n, z2n, z3n, z1d, z2d, and z3d).

A. Atmospheric Radiance

The atmospheric limb radiance component, calculated using the SAMM model for both day and night conditions with solar zenith angles of 43 and 137 deg for an equatorial model atmosphere, is shown in Fig. 3 for altitudes from 0 to 250 km. The atmospheric limb radiance profile is the model spectral radiance integrated over the SPIRIT III system spectral response function.

B. Zodiacal Radiance

Zodiacal LWIR infrared backgrounds, produced by the thermal emission of interplanetary dust particles in the solar system, were estimated for the SPIRIT III radiometer bands using CBZODY, the Celestial Background Zodiacal Emission model, described in Ref. 14. The zodiacal background, detected by the SPIRIT III LWIR bands, was a component in all MSX LWIR above the horizon observations. Zodiacal radiance is shown in Fig. 3 for three line-of-sight orientations relative to solar elongation and ecliptic latitude: 30° elongation and 0° latitude (z1), the 90° ecliptic latitude view (z2), and 180° elongation and 0° latitude (z3).

C. Nonrejected Earth Radiance

NRER was computed for each SPIRIT III radiometer band based on a formulation reported earlier (Dowling, J. M., Aerospace Corporation, private communication, 1984) and presented at SPIRIT III design reviews (Wong, D., Spectral Sciences, Inc., private communication 1986; Wyatt, C., Utah State University, private communication, 1986). NRER is given by the expression

$$\mathrm{NRER} = C \int_{\text{hemisphere}} \mathrm{PSRR}(\theta, \phi) L(\theta, \phi)\, \mathrm{d}\theta\, \mathrm{d}\phi \tag{1}$$

$$\mathrm{PSRR} = \left[\frac{A}{\theta^3}\right] + \left[\frac{B_1[1 - F(\theta)]}{\theta^{m_1}} + \frac{B_2[1 - G(\theta)]}{\theta^{m_2}}\right] + \left[\frac{B_1 k \cos\theta}{\theta^{n_1}} + \frac{B_2 k \cos\theta}{\theta^{n_2}}\right] \tag{2}$$

where C is a proportionality constant, $L\ (\theta, \phi)$ the terrestrial and atmospheric radiance from SAMM, and θ and ϕ the elevation and azimuth angles measured from the SPIRIT III optical axis or line of sight (LOS). B_1 and B_2 are the BRDF coefficients for the primary and secondary mirrors, and similarly the exponential terms m_1, n_1, m_2, and n_2 also refer to the primary and secondary mirrors, respectively.

For the NRER computation in the prelaunch simulation, it was assumed the PSRR is axially (azimuthally) symmetric and the off-axis angle is defined as elevation angles equal to or greater than 0.1 deg from the boresight of the SPIRIT III radiometer. The radiometer was capable of sweeping out a 1×3 deg field of regard in the mirror scan operating mode, and thus this off-axis definition, used for completeness in the calculation, extends into the actual field of regard. The PSRR given by Eq. (2) consists of three terms. The first term is caused by diffraction at the telescope aperture and has the theoretical form

$$\mathrm{PSRR(diffraction)} = \frac{A}{\theta^3} = \frac{\langle\lambda\rangle * (57.3)^3}{D * \mathrm{DSF} * (\pi\theta)^3}\ \mathrm{sr}^{-1} \tag{3}$$

where DSF is the diffraction suppression factor (2000 for SPIRIT III).

The diffraction term is independent of mirror condition (BRDF) and sets a minimum level of NRER caused by diffraction at the entrance aperture of the telescope. A Lyot stop, designed to image the entrance aperture, was modified[11] during optical tests of the SPIRIT III telescope to minimize scattered light, and the modification reduced the telescope aperture slightly to an effective diameter of 33.8 cm (Space Dynamics Laboratory, Utah State University, private communication, 1993).

The second term in Eq. (2) is caused by scatter from the primary and secondary mirror. Scatter, as measured by the BRDF, is caused by the physical condition of the mirror surface, including contamination from particulates and condensable molecular films. The second term includes the fraction of the primary and secondary mirrors that are illuminated, $[1 - F(\theta)]$ and $[1 - G(\theta)]$ as a function of the off-axis angle θ, where

$$F(\theta) = \theta/(\tan^{-1} D/L) \tag{4}$$

where D is the diameter of the collection aperture and L is the length of the telescope barrel, and

$$1 - F(\theta) = 0 \qquad \text{for} \qquad \theta/(\tan^{-1} D/L) > 1 \tag{5}$$

$$G(\theta) = \theta/4 \tag{6}$$

$$1 - G(\theta) = 0 \qquad \text{for} \qquad \theta/4 > 1 \tag{7}$$

The functions are zero at angles greater than 14 and 4 deg for the primary and secondary mirror, respectively. The 14-deg primary mirror limit is the extreme angle that directly illuminates the mirror as shielded by the telescope barrel assembly and mirror configuration; the 4-deg limit is the extreme angle that directly illuminates the secondary mirror.

The third term in Eq. (2) is caused by indirect or secondary scatter in the optical system and is termed the baffle cavity scattering function. The source is stray radiance that enters the telescope at off-axis angles up to 90 deg, is scattered from the surfaces, and baffles along the telescope barrel, and is scattered again from the primary and secondary telescope mirrors. The exponents m and n are related by

$$n = m - 1 \qquad \text{for} \qquad m > 1 \tag{8}$$

The quantity k is an empirically determined dimensionless secondary scatter suppression factor, and an estimated value of 2.2×10^{-4} was used in the prelaunch simulation. An Earth shield at the telescope aperture was used to limit terrestrial radiation entering the telescope at large angles to suppress this secondary source of stray radiation to the infrared sensor and reduce the thermal load on the cryogenic cooling system. The Earth shield was oriented in the nominal toward Earth position in the Earth limb measurements reported here.

The values of PSRR calculated for the SPIRIT III sensor are illustrated in Figs. 4–6 as a function of off-axis angle θ for the three levels

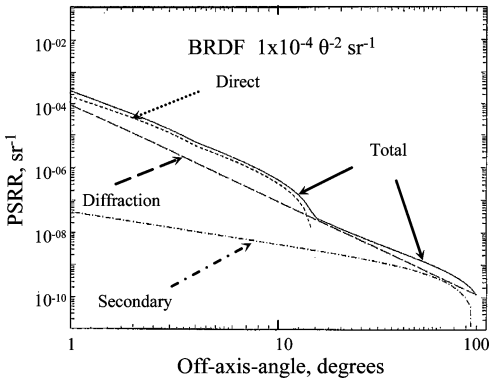

Fig. 4 Components of PSRR for the clean mirror case of Table 2. Components due to diffraction (diffraction), direct scatter from the primary and secondary mirrors (direct), and indirect or secondary scatter (secondary) are shown.

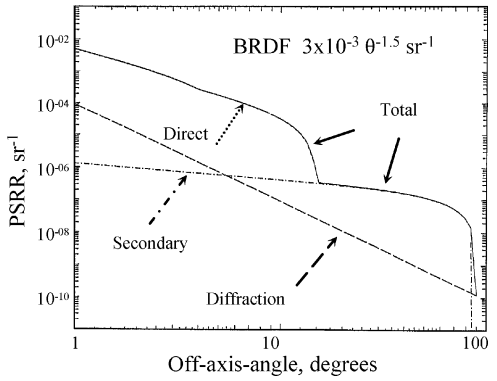

Fig. 5 Components of PSRR for the moderately contaminated case of Table 2.

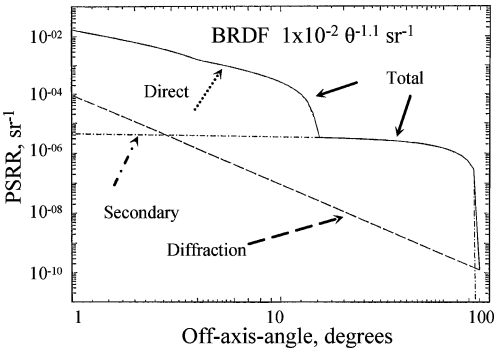

Fig. 6 Components of PSRR for the contaminated case of Table 2.

of BRDF given in Table 2 and the terms and parameters for diffraction and secondary scatter described in this section. Figures 4–6 indicate the contributions of each of the three components of PSRR as given in Eq. (2): diffraction, direct scatter from the primary and secondary mirrors (labeled direct), and indirectly scattered radiation (secondary). The BDRF values were assumed to be the same for both the primary and secondary mirrors. Figure 4 indicates that diffraction represents up to one-third of the total PSRR at small off-axis angles and is the major component of the PSRR at angles beyond 14 deg in the case of the very clean mirror. Diffraction contributes less than 2 and 0.5% to the PSRR at small angles and even less at larger angles in the more contaminated cases illustrated in Figs. 5 and 6. Scatter from the primary mirror is the major component of PSRR at off-axis angles up to 14 deg, the angular limit for direct illumination. At angles from 14 to 90 deg, secondary or indirect scatter is the major component of the PSRR for the contaminated mirror cases represented by Figs. 5 and 6.

NRER is the hemispherical integral of the atmospheric and terrestrial radiance weighted by the PSRR as indicated in Eq. (1). The NRER presented in Fig. 3 for band C, 11.1–13.2 μm, is based on a calculation of background radiance at 249 zenith angles from 30 to 180 deg, the nadir point. The Earth's horizon is observed at a zenith angle of approximately 118.8 deg from the MSX satellite altitude of 900 km. The zenith angles used in the NRER calculation increased in increments based on the magnitude of the gradients in the background radiance. Between zenith angles of 30 and 113 deg, a 1-deg increment was used. Beyond 113 deg, the zenith angles were defined by a 2-km decrement in tangent height from 298 km to the hard Earth. The final set of zenith angles represents the boresight pointed at the Earth's surface and is equivalent to negative tangent heights with the tangent altitudes varying from -1.0 to -6371.0 km and increasing incrementally by powers of 2. The integration was performed in the following manner. A given zenith angle corresponds to a particular line of sight from the spacecraft and also corresponds to a specific tangent altitude and background radiance. The PSRR was assumed to be azimuthally symmetric about the line of sight and was calculated for 36 preset elevation angles θ from the LOS. The values of θ used in the calculation were specified as follows: between 0.1 and 1.0 deg, the angle is increased in increments of 0.1 deg; the next four values were 1.2, 1.5, 2.0, and 2.5 deg; between 3 and 15 deg the angle was increased in increments of 1 deg; the next three values were 17.5, 20, and 25 deg; and finally from 30 to 90 the angle was increased in increments of 10 deg. At each of the indicated off-axis angles θ from the line of sight, an annular ring around the line of sight was portioned into 720 equal azimuthal segments ϕ. At each segment, a calculation was performed to determine the tangent height at that particular orientation ϕ in the annular ring at that off-axis angle θ. Once the tangent height was determined, the radiance for that tangent height was extracted from a predetermined altitude radiance profile as predicted by the SAMM model. The radiance values for the 720 segments were summed, averaged, and multiplied by the PSRR factor for that off-axis angle θ, as well as the cosine of the off-axis angle to take into account that the radiance is not normal to the optical axis. The final step of the integration sums the radiance contributions for each of the annular rings to determine the NRER using a trapezoidal summation method. The calculation was performed for a range of boresight zenith angles to provide an estimate of NRER as a function of tangent altitude as shown in Fig. 3.

Calculated values of NRER are presented for band C, 11.1–13.2 μm, in Figs. 7–9 for each of the levels of mirror contamination specified in Table 2, the PSRR values in Figs. 4–6, and the radiance given by SAMM for a cloud-free equatorial night atmosphere. The figures present NRER as a function of elevation angle and illustrate the contribution attributed to the atmosphere (the ATH component) and the combined Earth's surface and atmosphere (the BTH component). As can be seen, the BTH term is the dominant

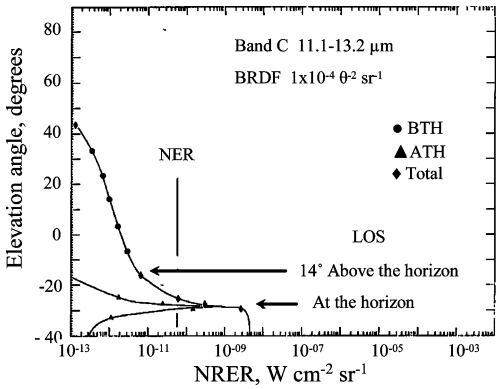

Fig. 7 NRER for band C (11.1–13.2 μm) for the pristine mirror case. The atmospheric (above the horizon; ATH) and terrestrial (below the horizon; BTH) components of NRER are shown as a function of the SPIRIT III boresight elevation angle above the spacecraft local horizontal. The noise equivalent radiance (NER) of the radiometer band is indicated.

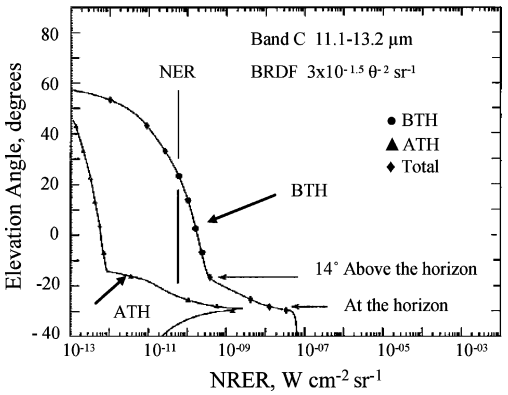

Fig. 8 NRER for band C for the moderately contaminated mirror case.

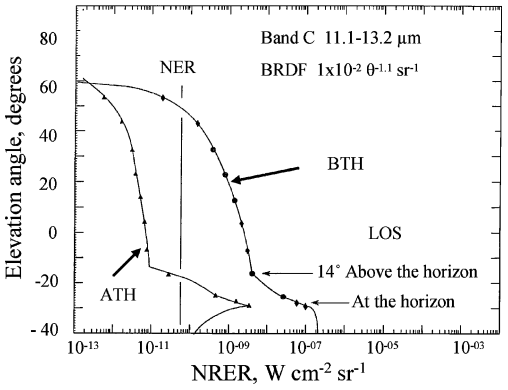

Fig. 9 NRER for band C for the contaminated mirror case.

source of NRER in Figs. 7–9. The atmospheric contributions are small. However, the atmosphere does modify the radiation from the hard Earth and has a profound effect on the MSX band D, which is centered on the optically thick 15-μm atmospheric CO_2 band. The noise equivalent radiance for band C in the most sensitive gain state is approximately 5×10^{-11} W cm^{-2} sr^{-1} and is indicative of the detection threshold for the measurement of NRER. From the MSX altitude of 900 km, the Earth subtends an angle of approximately 122 deg, and the Earth's horizon is located at an angle of 28.8 deg below the local horizontal direction at the spacecraft. The effect of radiance from the Earth's horizon directly illuminating the primary mirror at the extreme off-axis angle of approximately 14 deg is apparent in Figs. 7–9 as a sharp increase in NRER at a boresight elevation angle of minus 14.8 deg, equivalent to a tangent height of 660 km for a sensor at 900 km. NRER continues to increase at lower elevation angles as more of the primary mirror is illuminated by the Earth's surface. At an elevation angle of approximately −28.8 deg, the boresight is pointed at the horizon, and at more negative angles the atmospheric component of NRER decreases as the ATH region fills less, and the BTH component increases as it continues to fill more of the off-axis field of view.

III. MSX Prelaunch BRDF Data Measurements

Prelaunch measurements indicated, even with stringent cleanliness precautions and procedures, particles were deposited on the primary mirror during handling and testing, and some level of particle accumulation on the primary mirror of the SPIRIT III sensor was anticipated as a source of NRER at higher altitudes in the Earth limb experiments. By using high-quality optics, mirror surface roughness was not a significant source of stray light in the SPIRIT III sensor. The range of BRDF values measured for the SPIRIT III primary mirror during the prelaunch period from 1991 to the April 1994 is reviewed and discussed in Ref. 15. The preflight BRDF measurements of the assembled instrument were made with a portable BRDF station using a 10.6-μm CO_2 laser that sampled a small section of the primary mirror over a limited, 4- to 9-deg, range of angles from the specular direction. The values extrapolated to a 1-deg off-axis angle ranged from $3.2 \times 10^{-4} \times \theta^{-3.0}$ sr^{-1}, measured in a bench test of the clean primary mirror, to $1.2 \times 10^{-3} \times \theta^{-1.43}$ sr^{-1}, measured on the assembled instrument after extensive handling during shipment to California and return to Utah. Between periodic disassembly and cleaning, the BRDF of the primary mirror in the assembled instrument degraded over time.[15] The BRDF coefficient (the B term in Table 2) continued to increase with time, but the angular roll off approached and somewhat stabilized at a value of approximately $\theta^{-1.5}$. Inspection indicated particulates were the major contaminant in the preflight assembly and test period. Periodic cleaning restored the mirror to its pristine initial conditions. The final prelaunch measurement (Space Dynamics Laboratory, Utah State University, private communication, 1998) of the primary mirror BRDF, taken in November 1995 with the portable BRDF station 10.6-μm CO_2 laser and extrapolated to one degree, was $2.7 \times 10^{-4} \times \theta^{-2.2}$ sr^{-1}.

IV. Contamination Studies and On-Orbit Measurements

Contaminants can be in the form of particulates or molecular films resulting from the condensation of volatile material on the SPIRIT III optics that were maintained at a temperature of approximately 10 to 20 K for an extended period prior to launch and for the 10-month period of on-orbit infrared measurements. The MSX satellite included an extensive complement of sensors to monitor the local spacecraft environment and contamination of spacecraft surfaces by condensed volatile gases[1] including a cryogenic quartz crystal microbalance (CQCM), located next to the SPIRIT III primary mirror to monitor cryofilm deposits. Prelaunch studies of the scattering effects of thin-film cryodeposits of nitrogen and water vapor were performed in laboratory facilities[16] to support the analysis of the on-orbit CQCM measurements and the performance of the SPIRIT III optical system.

A time-dependent model of molecular contamination on the satellite surfaces and in the local spacecraft environment produced by outgassing from the spacecraft materials and the return flux from interaction with the ambient atmosphere was developed[17] before launch to assist in determining the major sources of contamination. The outgassing model considered water vapor from the multilayer insulating blankets that cover much of the spacecraft surfaces, argon from the supply of solid argon used to cool the deployable telescope cover, potential gas leakage from the device used to release the SPIRIT III cover, hydrogen venting from the solid hydrogen cryogen in the SPIRIT III sensor, and other compounds from the spacecraft components.

The prelaunch time-dependent model estimates of water vapor, the dominant outgassing species, agreed reasonably well with the early MSX on-orbit measurements.[17] Removal of the SPIRIT III telescope aperture cover was delayed until the seventh day on orbit to allow decay of the water vapor contamination levels in the spacecraft environment and reduce the possibility of deposits on the cryogenic optical surfaces of the SPIRIT III sensor. The telescope cover, cooled to 87 K with solid argon to provide a cold background for the infrared sensor and to preserve the solid hydrogen main cryogen supply, was opened and ejected by the activation of a pyrotechnic device contained in a sealed assembly to minimize contaminants. The CQCM measurements and analysis as reported in detail in Refs. 18 and 19 are briefly summarized here. The CQCM temperature decreased from 28 to 21 K during the first seven days in orbit, and a small amount of molecular oxygen gradually accumulated on the CQCM prior to the cover opening from the redistribution of previously condensed gaseous oxygen emanating from the telescope baffle. A 72-Å layer of material, deposited on the CQCM in the 1-min interval following the cover release, was subsequently identified as argon by thermogravimetric analysis, a procedure that monitors the depletion rate of material mass on the CQCM surface as its temperature is slowly increased to specify the evaporation temperature, the species, and the approximate film thickness. During the 10 months of infrared measurements, very little additional condensable volatile material was deposited on the CQCM. A total

film thickness of 155 Å, consisting of oxygen and argon, was deposited on the CQCM from the time of prelaunch cooldown until the end of the SPIRIT III 10-month period of on orbit infrared measurements. Laboratory experiments[16] demonstrated cyrofilm layers of this thickness are several orders of magnitude too thin to significantly impact the LWIR reflection or stray radiation rejection properties of mirror surfaces, and these results combined with the CQCM measurements eliminate condensable molecular films on the primary mirror as a significant source of NRER in the on-orbit performance of the SPIRIT III sensor.

The CQCM senses the mass of material attached to an exposed quartz crystal by detecting a change in its resonant frequency, near 10 MHz, compared with a similar unexposed reference crystal. Condensable volatile materials form cryofilm depositions attached to the quartz crystal, change its mass and resonant frequency, and thus were detected by the CQCM. However, particulates that reside on the crystal surface as loose unattached material do not change its piezoelectric resonant frequency and were not detected by the SPIRIT III CQCM. The NRER observed in the SPIRIT III measurements is attributed to scatter from particulates on the telescope primary mirror.

V. On-Orbit NRER Measurements: Band A (6.8–10.8 μm)

Stray light from the lower atmosphere and terrestrial surface was observed in the SPIRIT III LWIR band measurements of the Earth limb at tangent heights in the range from approximately 100 to 900 km. In one type of Earth limb background measurement, nominally 20–30 min in duration, high-resolution images of the atmosphere were produced in a pushbroom scan by maintaining the columns of the SPIRIT III linear focal plane arrays in a vertical alignment, the line of sight in a plane normal to the spacecraft velocity and the boresight at a constant tangent height. The SPIRIT III radiometer contained five linear detector arrays with two to eight active columns of 192 pixels. The 192 pixels represented a total field of view of 1 deg, equivalent to an altitude range of 60 km and a resolution of approximately 0.3 km at tangent height altitudes of 30–150 km.

Figure 10 presents a 1-s data sample from a night measurement performed on 18 November 1996 with a boresight tangent height of 104 km located over the Philippine Islands. The band A (6.8–10.8 μm) limb radiance profile at tangent heights from 76 to 132 km is compared with calculations for the major components of limb radiance in the SPIRIT III measurements. Model calculations for atmospheric, zodiacal, and NRER are presented based on the SAMM[13] model for an equatorial night atmosphere, the CBZODY (Celestial Background Zodiacal) radiance model[14] for the solar elongation and ecliptic latitude of the measurement, and the SPIRIT III NRER assuming the moderately contaminated telescope mirror case given in Table 2, which has a BRDF value of $3.0 \times 10^{-3}\theta^{-1.5}$ sr^{-1}. The calculated NRER profile also assumes the terrestrial radiance given by the SAMM model for cloud-free equatorial scene with a surface emissivity of 0.6. The measured profile indicates a radiance peak of 7×10^{-7} W cm^{-2} sr^{-1} at 85 km caused by 9.6-μm chemiluminescent emission from the mesospheric ozone layer. The model in this case overestimates the atmospheric radiance with a larger but less pronounced peak in the ozone radiance layer. Atmospheric emission is the primary contributor to the measured limb radiance profile at altitudes less than approximately 100 km in Fig. 10, and the model indicates the atmospheric component decreases rapidly above 90 km to a level of approximately 1×10^{-11} W cm^{-2} sr^{-1} at 130 km. The model estimate for zodiacal radiance in Fig. 10 is 1.1×10^{-10} W cm^{-2} sr^{-1} and less than 1% of the measured limb profile in this altitude range. NRER is the dominant component of the 6.8–10.8-μm band limb radiance in Fig. 10 at altitudes above 110 km, and the BRDF value assumed here as a reference underestimates the measured NRER by approximately a factor of three.

In an experiment, designed as a constant tangent height pushbroom scan of the Earth limb at tangent heights in the range from 40 to 150 km and performed periodically during the 10 months of infrared measurements, radiance profiles were recorded in scans down from and up to 900 km at the start and end of each data collection event. Figures 11 and 12 illustrate limb radiance measured in tangent height scans from 900 to 80 and 80 to 900 km for the SPIRIT III A (6.8–10.8 μm) band at the start and end of a data collection event performed on 1 November 1996 over the Pacific Ocean near Chile (Fig. 11) and California (Fig. 12). The NRER profiles in Figs. 11 and 12 were analyzed by using basis functions for the components

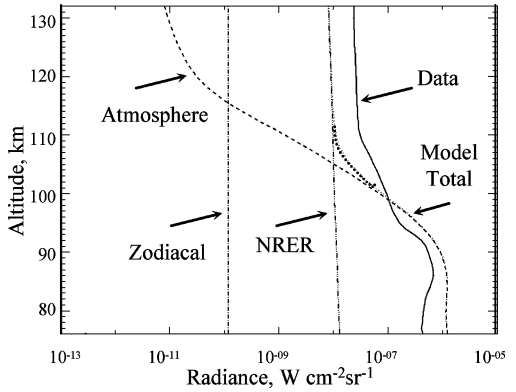

Fig. 10 Measured (data) and modeled limb radiance profiles for MSX band A (6.8–10.8 μm). Atmospheric radiance and NRER are the primary components of the limb radiance in this tangent height range.

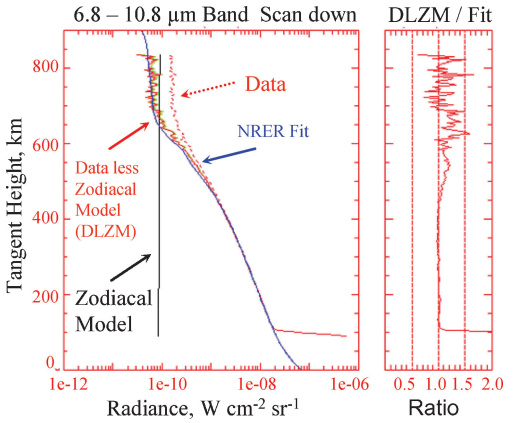

Fig. 11 Limb radiance profile data (shown as a dashed red line) for the MSX (6.8–10.8 μm) band at tangent heights from 100 to 900 km. The data less the model (black) of zodiacal radiance, DLZM, are shown as the solid red profile. The NRER model fit to the DLZM above 200 km is shown in blue. The sensor scanned from high to lower altitudes in this measurement. The ratio of the DLZM to the NRER model fit above 200 km is shown in the right panel.

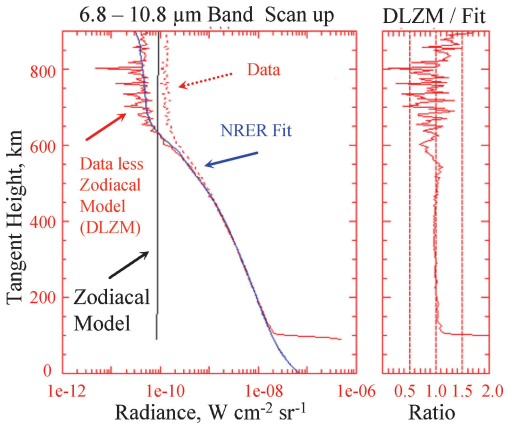

Fig. 12 Similar to Fig. 11 for data recorded at the conclusion of the same data collection event as the sensor scanned from low to higher altitudes.

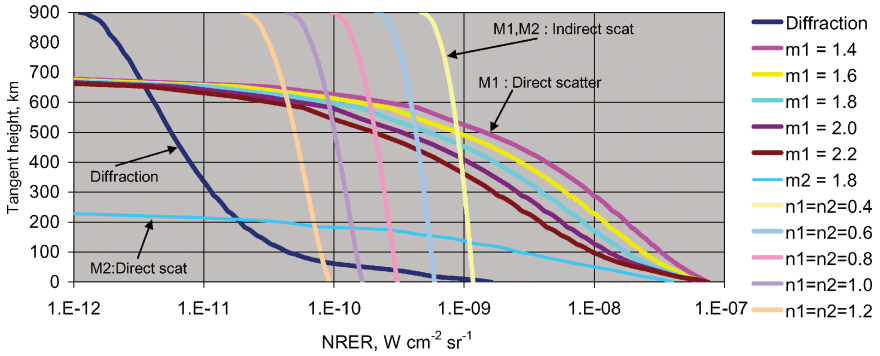

Fig. 13 Values of band A NRER components and exponents used to fit profiles at tangent heights from 200 to 900 km. M1 and M2 refer to the primary and secondary SPIRIT III telescope mirrors.

Table 3 BRDF exponent values for NRER component basis functions[a]

Component description	i	Values
Direct scatter, primary mirror	$m1$	1.4, 1.6, 1.8, 2.0, 2.2
Direct scatter, secondary mirror	$m2$	1.4, 1.6, 1.8, 2.0, 2.2
Indirect scatter, primary mirror	$n1$	0.4, 0.6, 0.8, 1.0, 1.2
Indirect scatter, secondary mirror	$n2$	0.4, 0.6, 0.8, 1.0, 1.2

[a]BRDF $= 1.0 \times 10^{-2} \times \theta^{-i}$ (sr^{-1}).

of NRER described in Eqs. (1) and (2), diffraction and direct and indirect scatter from the primary and secondary mirrors, and presented in Fig. 13 for band A (6.8–10.8 μm) for tangents heights from 0 to 900 km for a BRDF coefficient of 1.0×10^{-2} and a range of values for the exponent of the angular dependence term. The BRDF coefficient in Fig. 13, 1.0×10^{-2}, was selected as a nominal value for the 6.8–10.8-μm band based on the initial fits to a number of limb radiance profiles similar to Figs. 11 and 12. The values for primary and secondary mirror BRDF exponential terms that were used to generate the NRER components in Fig. 13 are defined in Table 3 and were selected to exceed the range of possible fits to the NRER measurements. The NRER components have unique altitude profiles in the range from 100 to 900 km, and direct scatter from the primary mirror is the dominant source of NRER in the altitude range from 100 to approximately 550 km. The diffraction component of NRER, based on the parameters described earlier and represented in Figs. 4–6, is much smaller than the direct and indirect mirror scatter components in Fig. 13 at all altitudes. NRER caused by direct scatter from the secondary mirror falls rapidly with altitude and at tangent heights of 200 km or more contributes less than 1% of directly scattered off-axis radiance from the primary mirror. No measurable contribution to NRER from the secondary mirror was indicated in this analysis. At altitudes above approximately 660 km, Figs. 11 and 12 indicate the measured band A (6.8–10.8 μm) radiance profiles approach nearly constant values of 1–2 $\times 10^{-10}$ W cm^{-2} sr^{-1}. In this altitude range the telescope barrel shields the primary mirror from direct illumination by the Earth's surface, and the measured radiance is caused primarily by the zodiacal background as indicated in Figs. 11 and 12. The model CBZODY has been used to estimate and remove the zodiacal background level from limb radiance profiles used in the NRER analysis reported here. Figures 11 and 12 indicate that after removal of the zodiacal component a radiance level of approximately 4–6 $\times 10^{-11}$ W cm^{-2} sr^{-1} is present above 600 km. This level is close to the detection threshold for the 6.8–10.8-μm band lower gain state data in Figs. 11 and 12 and is attributed to indirect scatter from the telescope mirrors and or residual uncorrected dark current. Fits to the NRER data illustrated in Figs. 11 and 12, based on Eqs. (1) and (2) and the basis functions presented in Fig. 13, provided primary mirror values for BRDF of $1 \times 10^{-2}\,\theta^{-1.74}$ and $1 \times 10^{-2}\,\theta^{-1.76}$ sr^{-1} at 1 deg and upper-limit estimates of 6.0×10^{-5} and 5.0×10^{-5} for k, the dimensionless secondary scatter suppression factor.

The accuracy of the BRDF coefficient is based on the validity of the SAMM model of low-altitude atmospheric and surface radiance for a specific measurement. In this instance, the model assumed an LWIR emissivity of 0.6 for the ocean surface and cloud-free conditions. The emissivity is an approximate value for a water surface observed at large zenith angles, which is the case for the direct scatter from the primary mirror in this measurement. Radiance from the terrestrial surface near the horizon, observed at smaller off-axis angles, is a heavily weighted component of NRER caused by rapid decrease in BRDF at larger angles. The presence of tropospheric clouds near the horizon, colder than the terrestrial surface, reduces the level of the NRER, and their intermittent nature produced a low-frequency cloud induced modulation of the NRER observed as a correlated feature in the band A, C, and E Earth limb measurements at tangent heights above 100 km. As noted, NRER is below the detection threshold of band B, and band D does not detect cloud altitudes because of the optical opacity of the 15-μm CO_2 band. An erroneous assumption of cloud-free conditions would lead to BRDF values less than the actual values. Several considerations were given to increase the probability that cloud-free conditions were present in the NRER data selected for the analysis reported here. Data collection events were selected that showed little or no cloud-induced band A, C, and E NRER modulation in the constant tangent height scan time periods immediately after and before NRER limb profiles generated in scans down from and up to 900 km. The cloud climatology reported by Wylie et al.[20] was used to select events where cloud-free conditions were highly probable. Finally, a number of measurement events were analyzed for each LWIR band to increase the number of samples and to identify and exclude the events that indicate the presence of clouds in the off-axis scene based on lower values of BRDF in bands A, C, and E compared to band D.

VI. On-Orbit NRER Measurements: LWIR Bands

Figure 14 presents 100- to 900-km tangent height profiles for the four LWIR bands measured simultaneously over the Indian Ocean of the northwest coast of Australia at the conclusion of the constant tangent height experiment performed on 18 November 1996, which is also illustrated in Fig. 10. NRER is the dominant component of limb radiance in all bands from 160 to 550 km, whereas bands A and D show contributions from atmospheric emission at altitudes less than 100 and 160 km. Figure 14 indicates that the NRER decreases with altitude at essentially the same rate in bands A and C, at a greater rate in D and an even greater rate in E, a consistent trend in the data attributed to the wavelength dependent angular scattering properties of the primary mirror contaminants.

The limb radiance profiles illustrated in Fig. 14 were generated by scanning the SPIRIT III sensor to higher altitudes. As the boresight moves to higher tangent heights, a decreasing fraction of the mirror surface is illuminated by the Earth's disk up to a tangent height of approximately 660 km where the horizon, vignetted by the telescope

Table 4 BRDF values the SPIRIT III primary mirror for LWIR radiometer bands[a]

Band, μm	Events	B	m
A, 6.8–10.8	6	$1.11 \pm 0.22 \times 10^{-2}$	1.71 ± 0.07
C, 11.1–13.2	6	$1.03 \pm 0.05 \times 10^{-2}$	1.66 ± 0.10
D, 13.5–15.9	4	$2.21 \pm 0.18 \times 10^{-2}$	2.04 ± 0.21
E, 18.2–25.1	2	$2.59 \pm 0.02 \times 10^{-2}$	2.10 ± 0.09

[a]BRDF $= B \times \theta^{-m}$ (sr^{-1}).

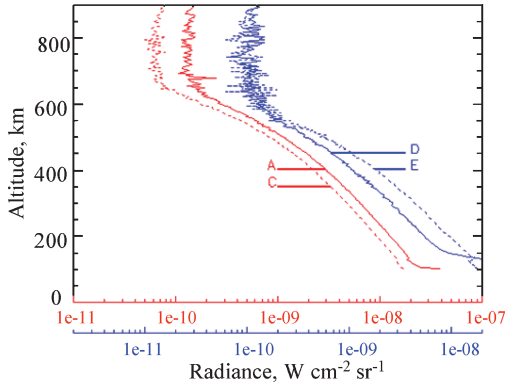

Fig. 14 Earth limb radiance profiles for the LWIR bands, A (6.8–10.8), C (11.1–13.2), D (13.5–15.9), and E (18.2–25.1) μm, measured over the Pacific Ocean of the coast of California on 1 November 1996. The upper radiance scale (red) applies to bands A and C and the lower (blue) scale to bands D and E.

assembly and entrance aperture, directly illuminates only the upper edge of the primary telescope mirror. The NRER component in the radiance profiles in Fig. 14 is produced by scatter from particulates from a range of mirror surface areas and the density, material, index of refraction and particle size distribution can differ over the mirror surface. The observations, recorded simultaneously in the four radiometer bands, represent NRER measured in scans of the Earth limb with the telescope Earth shield in its nominal toward Earth position. The BRDF values determined here are effective values assuming the particle contaminants are uniformly distributed over the primary mirror surface. The off-axis radiance gradients differ as determined by the atmospheric and terrestrial emissions and optical thickness of dominant molecular species in each band. The off-axis radiance distribution is treated in the analysis by the SAMM model with the assumptions that cloud-free conditions prevailed in the selected data events and a given measurement is accurately represented by mean model atmospheric temperatures, densities, and composition for the measurement time and location.

NRER limb radiance profiles at tangent heights up to 900 km, similar to Fig. 14 and measured at the start and conclusion of constant tangent height experiments, have been analyzed for each of the four SPIRIT III LWIR bands for a number of data collection events. Six data collection events were selected for analysis where cloud-free conditions were indicated by lack of modulation in the NRER data and cloud-free conditions were present for the location and date in question with monthly statistical probabilities between 60 and 82% (Ref. 20). In some cases, the band D and E radiance profiles indicated the high-altitude data were invalid because of artifacts such as dark current drift. The invalid data have been excluded from this analysis, reducing the number of analyzed events to four and two for bands D and E as shown in Table 4. The solar elongation angle and ecliptic latitude were determined for the profiles in each data collection event and used with the CBZODY model to determine and remove the zodiacal background from the LWIR limb radiance measurements. Limb radiance profiles above 200 km were analyzed to treat the data consistently for the four LWIR bands and to avoid contributions from atmospheric 15-μm CO_2 emissions in band D (13.5–15.9 μm). The radiance profiles for the data collection events referenced in Table 4 were fitted with a series of basis functions for both the coefficient and exponent in the BRDF term. The fit used an error minimization method (presented in the Appendix) that also provided an estimated error in the "goodness of fit." The error minimization method provided a primary mirror BRDF value of $1.1 \times 10^{-2}\,\theta^{-1.78}$ sr^{-1} for the 6.8–10.8-μm band limb measurement illustrated in Fig. 12. The accuracy of the BRDF coefficients is based on the validity of the SAMM model of atmospheric and surface radiance for a given measurement. The exponential term is determined by the gradient or slope of NRER with altitude, and the analysis, less dependent on the absolute radiance, assumes the off-axis scene content is uniform.

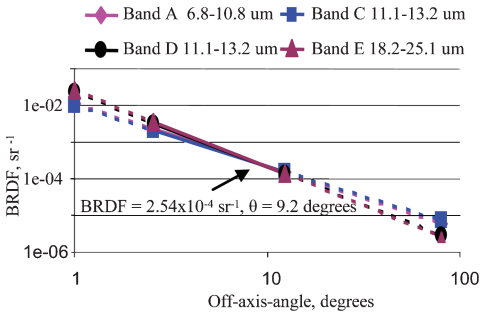

Fig. 15 BRDF values for the LWIR bands as summarized in Table 4 indicating convergence to approximately 2.5×10^{-4} at an of-axis angle, θ, of 9.2 deg. The BRDF values derived in this analysis were based on NRER data observed over the range of off-axis angles, 3–14 deg, indicated by the solid lines.

Table 4 indicates the number of data collection events analyzed for each spectral band and presents the mean values and standard deviations for the BRDF coefficients and exponential terms. The six measurements for bands A and C were performed during the period from 19 June to 18 November 1996. The ratio of the standard deviation to mean for the BRDF coefficient was 19, 5, 8, and 0.8% for bands A, C, D, and E, respectively, with no perceptible trend over the measurement period. The consistency of the results for bands A, C, and E suggests clouds were not a strong off-axis presence in any of the measurements selected for analysis and no measurable change was observed in the BRDF over the period from June to November 1996. An upper-limit estimate for any change in BRDF is 10%. The BRDF results summarized in Table 4 are illustrated in Fig. 15; the highlighted region from approximately 3 to 14 deg represents off-axis angle of primary mirror illumination by the Earth's surface at boresight tangent height altitudes in the range from approximately 180 to 600 km, the altitude region of the definitive MSX NRER measurements. The NRER in SPIRIT III radiometer is attributed to scattered radiation from particulates on the primary mirror that is reflected from the primary mirror into the optical sensor such that the scatter angle is the forward scatter angle and is equivalent to the off-axis angle of the source of the stray radiation. Extrapolated BRDF values are given in Fig. 15 for angles outside the range from 3 to 14 deg. The results in Table 4 show no measurable difference in the 6.8–10.8- and 11.1–13.2-μm bands based on the analysis of six data collection events and an increase in both the coefficient and the magnitude of the exponential term for the longer wavelength 13.5–15.9- and 18.2–25.1-μm bands based on four and two events, respectively. A bimodal distribution of BRDF with spectral band is evident in Table 4 and Fig. 15, which also illustrates the BRDF values for the four LWIR bands converge to a value of approximately 2.5×10^{-4} sr^{-1} at an of axis angle of 9.2 deg. Several effects could contribute to the spectral dependence of the NRER data evident in Fig. 14 and the derived BRDF values illustrated in Fig. 15. These include the complex index of refraction of the contaminant material or materials on the primary mirror, the size distribution(s) of the particulates over the primary mirror surface, and polarization of the scattered radiation and the polarization response functions of the LWIR interference filters, beam splitters, optics and detectors. The cause of the BRDF spectral dependence has not been identified in this analysis.

The out-of-field-of-view rejection properties of the SPIRIT III sensor were also characterized by the MSX Data Certification and Technology Transfer (DCATT) principal investigator team in experiments designed as dedicated measurements of NRER and nonrejected lunar radiation. The NRER measured in DCATT experiments at tangent heights from 100 to 900 km were compared as a function of roll or azimuth angle for each of the four SPIRIT III LWIR radiometer bands. Twelve NRER profiles are reported (Jayaraman, Sumita, Vanguard Research, Inc., 1999, private communication) for measurements obtained in azimuth or roll angle increments of approximately 30 deg in four tangent height scans in each of three data collection events over an 11-day period in May 1996. The NRER profiles show a minimum at the zero roll angle orientation (telescope entrance shield toward Earth) and local maxima roughly ±90 and 180 deg from that position. The results indicate a maximum NRER that is approximately 1.5 times larger than the minimum in all of the MSX LWIR spectral bands. These NRER limb profiles were recorded in 3-min scans at 5-min intervals over a number of days and some variations in NRER might be caused by changes in the off-axis scene radiance including the reduced thermal signatures associated with clouds. The DCATT team did report (Murdock, T. L., Frontier Technology, Inc., 1998, private communication) glint at some roll angles. However, the solid angle subtended by these glints is too small to influence the NRER significantly.

The BRDF of the SPIRIT III telescope was determined for the 6.8–10.8-μm band based on measurements of NRLR using the moon as a quasi point source. In this experiment the PSRR was measured directly as the SPIRIT III boresight scanned across the moon at a number of azimuth angles. The DCATT team reported (Murdock, private communication) a primary mirror BRDF (1 deg) of $1.56 \times 10^{-2}\,\theta^{-1.71}$ sr^{-1} for the 6.8–10.8-μm band based on analysis of July 1996 NRLR measurements at off-axis angles of 4 to 9 deg. DCATT team analysis of a similar lunar measurement in January 1997 resulted in PSRR levels 15% larger at angles less than 4 deg. In their analysis of the PSRR, the MSX DCATT team used the more appropriate expression for the illuminated area of the primary mirror than the linear function of the off-axis angle used in the present analysis. The DCATT analysis derived the area between the circle defined by the primary mirror and one representing the baffle offset from the primary circle center by the off-axis angle. This illumination expression falls a bit faster with off-axis angle than that used in the present analysis, which might contribute to the slight difference in the BRDF coefficients. However, the agreement between the 6.8–10.8-μm band BRDF exponential terms derived from the DCATT NRLR data and the result derived from the NRER analysis reported here and presented in Table 4 provides independent support for the current results, including those in the longer wavelength bands, which the DCATT team did not analyze.

VII. Discussion

The scatter of electromagnetic radiation by molecules and particles was initially described in Ref. 21. Mie theory describes the intensity, polarization, and angular distribution of scattered radiation from molecules and particles and is discussed and treated with comprehensive atmospheric applications in Refs. 22–25. Scatter from particles is controlled by the wavelength of incident radiation, the particle size distribution, and the complex index of refraction of the scattering particles. The dimensionless particle size parameter x is defined as

$$x = 2\pi r/\lambda \tag{9}$$

where r is the particle radius and λ the wavelength of the radiation. When x is much less than unity, Mie theory states the angular distribution and polarization effects of scattered radiation reduces to the Rayleigh scattering case and is characterized by an intensity inversely proportional to the fourth power of the radiation wavelength. The relatively small spectral dependence of the BRDF values derived here for four LWIR bands spanning a factor of approximately three in wavelength indicates the particle size parameter is unity or greater, and thus particles with diameters larger than 10 μm are the dominant source of NRER in the SPIRIT III telescope.

Laboratory studies of scattered radiation from particulates on mirror surfaces are described in Ref. 26 and in a series of papers, Refs. 27–30, in which measurements under controlled conditions are compared with Mie scatter theory as a function of material, particle size distribution, and wavelength. The BRDF of mirrors contaminated with dust particles with known polydisperse particle size distributions are reported[30] for scatter angles from 1 to 90 deg at several wavelengths as a function of contamination degree expressed as a surface cleanliness level based on the convention described in Ref. 31. The BRDF value derived here for the SPIRIT III 6.8–10.8-μm band for scatter angles of approximately 2 to 14 deg, given in Table 4, is between values reported[30] for laboratory measurements of 10.6-μm radiation scattered from mirrors with a cleanliness levels of 200 and 500. It is estimated that the current SPIRIT III 6.8–10.8-μm value is approximately equivalent to the radiation scattered from a mirror surface with cleanliness level 250 based on the reported results[30] for dust particles at room temperature and the particle distributions given in Ref. 31. The exceedance distribution of 0.1–100-μm particles, given in Ref. 31 for cleanliness level 250, shows approximately 6 and 0.3 particles per cm^2 with diameters greater than 20 and 60 μ, respectively. Other size distributions[32,33] have been proposed as more appropriate for optical surfaces contaminated by exposure to laboratory clean-room environments. Mie theory indicates and laboratory experiments[27–30] demonstrate that a few large particles dominate the scattered radiation from a distribution of particles that include sizes larger than the radiation wavelength.

The increased SPIRIT III primary mirror BRDF values reported here, approximately two orders of magnitude greater than the last prelaunch measurement, are attributed to particle accumulation on the mirror: during launch preparations, during the stressing vibrational environment of launch, and during the SPIRIT III cover opening process activated by a pyrotechnic device. The primary mirror BRDF values increased with time during the sensor prelaunch testing period because of particulate contamination. However, the magnitude of the BRDF values observed during the prelaunch testing period[15] was substantially smaller than the results derived in this analysis from the on-orbit measurements. The redistribution of particles as a result of the vibroacoustic shock and acceleration environment of a spacecraft launch is described and modeled in Ref. 34 using a generic Mars landing mission as an example. The SPIRIT III telescope mirror was oriented horizontally, facing upward and vulnerable to contamination by the redistribution of particles from downward-facing surfaces within the telescope assembly by the forces of axial acceleration during launch of the solid-fuel Delta II rocket engine. It is postulated that during launch the forces of acceleration and vibration released a significant number of particles from the downward-facing telescope cover and other surfaces inside the telescope assembly and these deposited on the primary mirror at the lower end of the telescope assembly.

VIII. Conclusions

The SPIRIT III sensor on the MSX satellite observed stray radiation from the terrestrial surface, NRER, at angles of approximately 2 to 14 deg from the optical axis in experiments designed to measure LWIR atmospheric limb emissions. The NRER observed in a series of Earth limb measurements in which the four LWIR radiometer bands simultaneously recorded radiance profiles at tangent heights from 150 to 900 km has been analyzed using the SAMM (SHARC and MODTRAN merged) model of atmospheric and terrestrial radiance to estimate the point source rejection ratio (PSRR) of the SPIRIT III optical system. The Earth limb radiance profiles were selected for analysis where the assumption of cloud-free conditions in the off-axis terrestrial scenes was supported by the absence of cloud-induced modulation in MSX NRER data and was also indicated to be highly probable by cloud climatology. Examination of components of the PSRR indicates that direct scatter of terrestrial radiance from contaminants on the telescope primary mirror is the dominant source of NRER and the bireflectance distribution function (BRDF) of the primary mirror for the SPIRIT III 6.8–10.8-μm radiometer band is $(1.11 \pm 0.22) \times 10^{-2}$ per sr at 1 deg off axis with

an off-axis angular dependence of $\theta^{-1.71\pm0.07}$. Similarly, the BRDF values for the three other long wavelength infrared (LWIR) radiometer bands (11.1–13.2, 13.5–15.9, and 18.2–25.1 μm) have been determined as $(1.03 \pm 0.05) \times 10^{-2}\,\theta^{-1.66\pm0.10}$, $(2.21 \pm 0.18) \times 10^{-2}\,\theta^{-2.04\pm0.21}$, and $(2.59 \pm 0.02) \times 10^{-2}\quad \theta^{-2.10\pm0.09}$ per sr. The BRDF results for the four SPIRIT III LWIR radiometer channels, based on an analysis that assumes the contamination is uniform in density and size distribution across primary mirror surface, converge to a common value of approximately 2.5 10^{-4} sr^{-1} at an off-axis angle of 9.2 deg. The results show a bimodal distribution with spectral band, no measurable difference in the 6.8–10.8- and 11.1–13.2-μm bands based on the analysis of six data collection events and an increase in both the coefficient and the magnitude of the exponential term for the longer wavelength 13.5–15.9- and 18.2–25.1-μm bands based on four and two events, respectively. The spectral dependence of the NRER data and the BRDF values derived in this analysis is attributed to the small angle, 2–14 deg, scattering characteristics of the particulates contaminating the primary mirror and perhaps any differences in the system spectral response functions for isotropic and polarized radiation for the SPIRIT III LWIR bands. Properties that might contribute to the observed spectral dependence include the complex index of refraction of the contaminant material or materials on the primary mirror, the size distribution(s) of the particulates over the primary mirror surface, and polarization of the scattered radiation and the response functions of the LWIR interference filters, beam splitters, optics, and detectors for polarized radiation.

The BRDF value derived from the on-orbit 6.8–10.8-μm band NRER data is substantially greater than the prelaunch measurements with a 10.6-μm laser. The increase is attributed to particulate accumulation on the primary telescope mirror during the extended launch-preparation period after the final mirror cleaning, during the stressing acceleration and vibrational launch environment with the mirror oriented horizontally and vulnerable to the redistribution of particles within the sensor and during the SPIRIT III cover opening process activated by a pyrotechnic device. It is postulated that during the forces of acceleration and vibration encountered in launch a significant number of particles were released from the downward-facing telescope cover and other surfaces inside the telescope assembly and accumulated on the primary mirror at the lower end of the telescope assembly. Mie scatter theory and the relatively small spectral dependence of the derived BRDF terms indicate scattered radiation from particles with diameters larger than 10 μ is the primary source of NRER in the SPIRIT III telescope. The BRDF values are approximately equivalent to the scattered radiation produced by a surface cleanliness level of 250 as defined by Military Standard 1246B. No measurable change in BRDF was observed during the observation period of the reported NRER measurements, 19 June to 18 November 1996; change in BRDF, if any, was less than 10%.

Appendix: Fitting Algorithm

NRER is given by Eqs. (A1) and (A2). Specifically,

$$\mathrm{NRER} = C \int_{\text{hemisphere}} \mathrm{PSRR}(\theta, \phi) L(\theta, \phi)\, \mathrm{d}\theta\, \mathrm{d}\phi \tag{A1}$$

$$\mathrm{PSRR} = \left[\frac{A}{\theta^3}\right] + \left[\frac{B_1[1 - F(\theta)]}{\theta^{m_1}} + \frac{B_2[1 - G(\theta)]}{\theta^{m_2}}\right] + \left[\frac{B_1 k \cos\theta}{\theta^{n_1}} + \frac{B_2 k \cos\theta}{\theta^{n_2}}\right] \tag{A2}$$

where PSRR is the point source rejection ratio per unit solid angle, L (θ, ϕ) the radiance from the SAMM model of atmospheric and terrestrial radiance, and θ and ϕ the elevation and azimuth angles measured from the SPIRIT III optical axis or line of sight. B1 and B2 are the BRDF coefficients for the primary and secondary mirrors, and similarly the exponential terms $m1$, $n1$, $m2$, and $n2$ also refer to the primary and secondary mirrors, respectively.

The BRDF coefficients and exponents are estimated by evaluating the integral in Eq. (A1) for a series of boresight elevation angles and fitting the resulting function of elevation angle to MSX radiometer measurements taken as the telescope scanned through a tangent altitude range of 100–900 km. The NRER function of elevation angle was transformed to a function of tangent altitude. The procedure used an error (goodness of fit) function, which was the rms of a quantity constructed by summing the data to model ratios for all of the data points in a selected tangent altitude range and subtracting unity. This function was evaluated over a grid of parameter values in which the fit function had a local minimum, which was taken as the best-fit parameter values.

A. Basis Functions

This multiparameter fitting process requires calculating the NRER function over a range of parameter values. The time required for these calculations is prohibitive, if the integral is evaluated directly for each set of parameter values. Instead the error function was evaluated with sufficient accuracy over the required set of parameter values by interpolating on a previously computed set of basis functions. The interpolation procedure permitted the rapid and accurate computation of NRER profiles for an arbitrary set of parameter values within the range of the selected grid.

The basis functions were constructed by integrating each of the five terms of PSRR (omitting the coefficient), multiplied by L, over the azimuth angle, ϕ, for a set of eight exponent values. This produced a set of 40 basis functions. The exponents were set: $m = m_1 = m_2$ and $n = n_1 = n_2 = m - 1$, which reduced the independent set of indices to one. The five functions were evaluated for eight increments of m from 1.0 to 2.4.

B. Accuracy of Interpolation

For a given set of parameter values, a set of eight profiles is computed by combining the five NRER components multiplied by a selected set of coefficients. Varying the B coefficients produced different linear combinations of the basis functions. A profile for a particular value of m is then obtained by interpolation. The accuracy of the interpolation was tested by eliminating each of the middle six profiles from the set and estimating it from the remaining profiles. A comparison of the estimated profile with the actual profile gave a maximum error of 0.07 for m values of 1.2 and 2.2. The fractional errors for the remaining profiles were less than 0.01. The error in

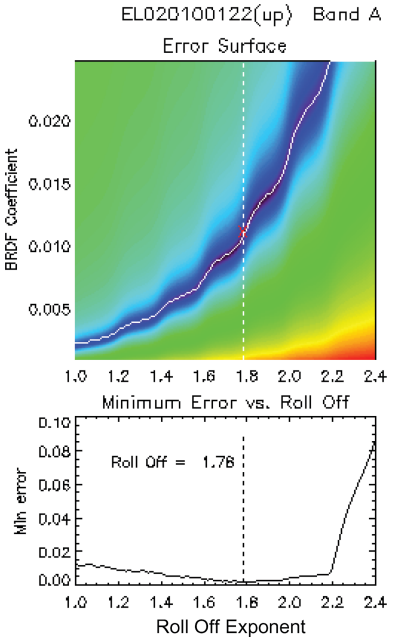

Fig. A1 Error matrix indicating the best fit to the data of Fig. 12 is a BDRF value of $1.1 \times 10^{-2}\,\theta^{-1.78}$ sr^{-1}.

the profile for $m = 2.2$ would lead to a consistent overestimation of the roll off of approximately 0.05, while the error in estimating the $m = 1.2$ profile would lead to underestimation of the roll off of approximately 0.05. These errors would be expected to be significantly larger than any resulting from estimating a profile using the complete set and are less than the standard deviation of the exponential terms derived from the multiple data events summarized in Table 4.

C. Error Matrix

The data profile was compared with the NRER model for a combination of parameter values by dividing the data values by the model and subtracting one. The rms value of these differences over a set altitude range was computed for each combination of parameters. The error matrix consisted of the set of these rms differences over the parameter grid. The minimum of the error function was located within a preset parameter grid instead of using a gradient-search algorithm designed to work with the tabulated basis functions due mainly to the nonmonotonic character of the error function. Minimizing the error over a preset grid assured that the absolute minimum of the error matrix was located. This is illustrated in Fig. A1 for the NRER measurement shown in Fig. 12.

Acknowledgments

The late Harold A. B. Gardiner formulated the approach and methodology used in the models and simulations of the components of limb radiance presented here and used in the analysis of the MSX measurements. His major contributions to this publication are respectfully and gratefully acknowledged. He is affectionately remembered for his technical insight, dedication, integrity, consistent good humor, and enduring friendship. A. T. Stair, the MSX Chief Scientist, currently affiliated with Visidyne, Inc.; John Mill, the MSX Project Scientist, currently of SpaceX Consulting; and Bruce Guilmain, the MSX Program Manager, currently with Utah State University, skillfully and adroitly directed, adapted, and managed the MSX program through several cycles of evolving missile defense requirements and concepts. Technical discussions with Steve Price, our colleague at the Air Force Research Laboratory, Ray Russell and Jerome Dowling of the Aerospace Corporation, Jim Dyer and Alan Thurgood of Utah State University, Manny Uy of the Applied Physics Laboratory, and Bobby Wood of Aerospace Consulting Services, Inc., contributed to our understanding of the contamination measurements performed on the SPIRIT III sensor and the effects of off-axis radiance on space-based cryogenic infrared optical systems.

References

[1]Mill, J. D., O'Neil, R. R., Price, S., Romick, G. J., Uy, O. M., Gaposchkin, E. M., Light, G. C., Moore, W. W., Murdock, T. L., and Stair, A. T., "Midcourse Space Experiment: Introduction to the Spacecraft, Instruments, and Scientific Objectives," *Journal of Spacecraft and Rockets*, Vol. 31, No. 5, 1994, pp. 900–907.

[2]O'Neil, R. R., Gardiner, H. A. B., Gibson, J., Humphrey, C. H., Hegblom, R., Fraser, M. E., and Kendra, M., "Midcourse Space Experiment (MSX): Planned Observations of Infrared Earthlimb and Terrestrial Backgrounds," AIAA Paper 96-0222, Jan. 1996.

[3]Dewan, E., Picard, R. H., O'Neil, R. R., Gardiner, H. A., Gibson, J., Mill, J. D., Richards, E., Kendra, M., and Gallery, W. O., "MSX Satellite Observations of Thunderstorm-Generated Gravity Waves in Mid-Wave Infrared Images of the Upper Stratosphere," *Geophysical Research Letters*, Vol. 25, No. 7, 1998, pp. 939–942.

[4]Picard, R., O'Neil, R., Gardiner, H., Gibson, J., Winick, J., Gallery, W., Wintersteiner, P., Hegblom, E., and Richards, E., "Remote Sensing of Discrete Stratospheric Gravity-Wave Structure in 4.3 Micron CO_2 Emission from the MSX Satellite," *Geophysical Research Letters*, Vol. 25, No. 15, 1998, pp. 2809–2812.

[5]Price, S. D., Egan, M. P., Carey, S. J., Mizuno, D., and Kuchar, T. A., "MSX Survey of the Galactic Plane," *Astronomical Journal*, Vol. 121, May 2001, pp. 2819–2842.

[6]Uy, O. M., Benson, R. C., Erlandson, R. E., Boies, M. T., Silver, D. M., Lesho, J. C., Galica, G. E., Green, B. D., Wood, B. E., and Hall, D. F., "MSX Contamination Instruments: Results of Gaseous and Particulate Environment versus Predictions," AIAA Paper 97-0315, Jan. 1997.

[7]Price, S. D., Paxson, C. P., Engelke, C., and Murdock, T. L., "Spectral Irradiance Calibration in the Infrared. XV. Absolute Calibration of Standard Stars by Experiments on the Midcourse Space Experiment," *Astronomical Journal*, Vol. 128, Aug. 2004, pp. 889–910.

[8]Smith, D. R., "Evidence for Off-Axis Leakage Radiance in High-Altitude IR Rocketborne Measurements," *SPIE Proceedings, Stray Light and Contamination in Optical Systems*, Vol. 967, edited by R. P. Breault, Society of Photo-Optical Instrumentation Engineers (International Society for Optical Engineering), Bellingham, WA, 1988, pp. 30–36.

[9]Wheeler, N. B., Smith, D., Dean, D., Gardiner, H., Gibson, J., Bates, L., Bingham, G., Johnson, K., Guregian, J., and Benoit, R., " An Assessment of the Near-Field Contamination and Off-Axis Leakage Effects on Earth-Limb Background Measurements from CIRRIS 1A," *Optical System Contamination: Effects, Measurement, and Control III*, Vol. 1754, edited by A. P. Glassford, Society of Photo-Optical Instrumentation Engineers (International Society for Optical Engineering), Bellingham, WA, 1992, pp. 156–168.

[10]Guregian, J. J., Benoit, R. T., and Wong, W. K., "An Overview of Contamination Effects on the Performance of High Straylight Rejection Telescopes via Ground Measurements," *Optical System Contamination: Effects, Measurement, and Control II*, Vol. 1329, edited by A. P. Glassford, Society of Photo-Optical Instrumentation Engineers (International Society for Optical Engineering), Bellingham, WA, 1990, pp. 2–15.

[11]Mastandrea, A. A., Glasheen, R. R., Guregian, J. J., and Esplin, R., "Development of the Spirit III Telescope; From Design Through Test," *Cryogenic Optical Systems and Instruments V*, Vol. 1765, edited by R. K. Melugin, Society of Photo-Optical Instrumentation Engineers (International Society for Optical Engineering), Bellingham, WA, 1992, pp. 41–52.

[12]Bartschi, B. Y., Morse, D. E., and Woolston, T. L., "The Spatial Infrared Imaging Telescope III," *Johns Hopkins APL Technical Digest*, Vol. 17, No. 2, 1996, pp. 215–225.

[13]Sharma, R. D., Brown, J. H., Berk, A., Acharya, P. K., Gruninger, J. H., Duff, J. W., and Sundberg, R. L., "Users Manual for SAMM, SHARC, and MODTRAN Merged," PL-TR-96-2090, ERP#1190, ADA, 310349, Hanscom AFB, April 1996.

[14]Noah, P. V., and Noah, M. A., "Validation Report for the Celestial Background Scene Descriptor (CBSD) Zodiacal Emission (CBZODY6) Model," Airforce Research Lab., AFRL-TR-2001-1578, Hanscom AFB, Feb. 2001.

[15]Dyer, J. S., Mikesell, R., Perry, R., Mikesell, T., and Guregian, J. J., "Contamination Measurements During Development and Testing of the SPIRIT III Cryogenic Infrared Telescope," *Optical Systems Contamination*, Vol. 2261, edited by A. P. Glassford, Society of Photo-Optical Instrumentation Engineers (International Society for Optical Engineering), Bellingham, WA, 1994, pp. 239–253.

[16]Wood, B. E., Seiber, B. L., Dertrand, W. T., and Uy, O. M., "Effects of Thin Cryo-Contaminant Films on Midcourse Space Experiment (MSX) Satellite Cryo-Optics," AIAA Paper 96-0221, Jan. 1996.

[17]Silver, D. M., Benson, R. C., Boies, M. T., Dyer, J. S., Erlandson, R. E., Galica, G. E., Green, B. D., Hall, D. F., Lesho, J. C., Phillips, T. E., Uy, O. M., and Wood, B. E., "Midcourse Space Experiment Molecular Contamination Modeling Predictions for Early Orbital Operations," *19th Space Simulations Conference: Cost Effective Testing for the 21st Century*, NASA CP 3341, 1967, pp. 67–78.

[18]Wood, B. E., Hall, D. F., Lesho, J. C., Uy, O. M., Boies, M. T., Silver, D. M., Benson, R. C., Dyer, J. C., Green, B. D., and Galica, G. E., "On-Orbit Midcourse Space Experiment (MSX) Satellite Environment Flight Experiments," AIAA Paper 99-0252, Jan. 1999.

[19]Wood, B. E., Hall, D. F., Lesho, J. C., Boies, M. T., Silver, D. M., Uy, O. M., Benson, R. C., Dyer, J. C., Galica, G. E., Green, B. D., and Bertrand, W. T., "MSX Satellite: Flight Measurements of Contaminant Films," AIAA Paper 98-2592, June 1998.

[20]Wylie, D. P., Menzel, W. P., Woolf, H. M., and Strabala, K. I., "1994: Four Years of Global Cirrus Cloud Statistics Using HIRS," *Journal of Climate*, Vol. 7, No. 12, 1994, pp. 1972–1986.

[21]Mie, G., "A Contribution to the Optics of Turbid Media, Especially Colloidal Metallic Suspensions," *Annals of Physics*, Vol. 25, No. 4, 1908, pp. 377–445 (in German).

[22]Van de Hulst, H. C., *Light Scattering by Small Particles*, Dover, New York, 1981.

[23]Kerker, M., *The Scattering of Light and Other Electromagnetic Radiation*, Academic Press, New York, 1969.

[24]McCartney, E. J., *Optics of the Atmosphere: Scattering by Molecules and Particles*, Wiley, New York, 1976.

[25]Coulson, K. L., *Polarization and Intensity of Light in the Atmosphere*, A. Deepak Publishing, Hampton, VA, 1988.

[26]Young, R. P., "Low-Scatter Mirror Degradation by Particle Contamination," *Optical Engineering*, Vol. 15, Nov.–Dec. 1976, pp. 516–520.

[27]Spyak, P. R., and Wolf, W. L., "Scatter from Particulate-Contaminated Mirrors, Part 1: Theory and Experiment for Polystyrene Spheres and $\lambda = 0.6328\ \mu$m," *Optical Engineering*, Vol. 31, No. 8, 1992, pp. 1746–1756.

[28]Spyak, P. R., and Wolf, W. L., "Scatter from Particulate-Contaminated Mirrors, Part 2: Theory and Experiment for Dust and $\lambda = 0.6328$ μm," *Optical Engineering*, Vol. 31, No. 8, 1992, pp. 1757–1763.

[29]Spyak, P. R., and Wolf, W. L., "Scatter from Particulate-Contaminated Mirrors, Part 3: Theory and Experiment for Polystyrene Spheres and $\lambda = 10.6$ μm," *Optical Engineering*, Vol. 31, No. 8, 1992, pp. 1764–1774.

[30]Spyak, P. R., and Wolf, W. L., "Scatter from Particulate-Contaminated Mirrors, Part 4: Properties of Scatter from Dust for Visible to Far-Infrared Wavelengths," *Optical Engineering*, Vol. 31, No. 8, 1992, pp. 1775–1784.

[31]Military Standard 1246B, "Product Cleanliness Levels and Contamination Control Program," 4 Sept. 1987.

[32]Dittman, G. D., "Contamination Scatter Functions for Stray-Light Analysis," *Optical System Contamination: Effects, Measurements, and Control VII*, Vol. 4774, edited by P. T. Chen and O. M. Uy, Society of Photo-Optical Instrumentation Engineers (International Society for Optical Engineering), Bellingham, WA, 2002, pp. 99–110.

[33]Peterson, R. V., Magallanes, P. G., and Rock, D. F., "Tailored Particle Distributions Derived From MIL-STD-1246," *Optical System Contamination: Effects, Measurements, and Control VII*, Vol. 4774, edited by P. T. Chen and O. M. Uy, Society of Photo-Optical Instrumentation Engineers (International Society for Optical Engineering), Bellingham, WA, 2002, pp. 79–98.

[34]Borson, E. N., "A Model for Particle Redistribution During Spacecraft Launch," *Optical System Contamination: Effects, Measurements, and Control VII*, Vol. 4774, edited by P. T. Chen and O. M. Uy, Society of Photo-Optical Instrumentation Engineers (International Society for Optical Engineering), Bellingham, WA, 2002, pp. 67–78.

A. Ketsdever
Associate Editor